JOURNAL OF SPACECRAFT AND ROCKETS
Vol. 34, No. 1, January–February 1997

Flight Data Analysis for the Photovoltaic Array Space Power Plus Diagnostics Experiment

James D. Soldi* and Daniel E. Hastings†
Massachusetts Institute of Technology, Cambridge, Massachusetts 02139
and
David Hardy,‡ Donald Guidice,‡ and Kevin Ray‡
U.S. Air Force Phillips Laboratory, Hanscom Air Force Base, Massachusetts 01731

As power demands continue to increase, spacecraft power systems are being designed to operate at higher voltages. When operating at high negative voltages, however, arcing may occur on the solar cells, generating electromagnetic interference and solar cell damage. Numerical and analytic models have been developed to simulate the arcing onset process, showing good agreement with experimental data. This simulation was used to predict arcing levels for the conventional geometry solar cells flown on the Photovoltaic Array Space Power (PASP) Plus experiment. Both preflight and postflight simulations showed good agreement with the flight data. The flight data were analyzed to examine correlations between arc rates and the various material, environmental, and operational parameters and to validate the theoretical model. Arcing levels were found to depend strongly on bias voltage, with the scalings suggested by the model proving to relate the arcing rates on the different modules accurately. Cell temperature was also verified as being a critical parameter, with high arcing rates seen at low temperatures. As expected from the model, there is a critical temperature, above which no arcing occurs. The ion flux was also seen to affect arc rates, as expected. Radiation flux to the arrays, however, did not affect arcing levels, although the data to support this conclusion are limited. Thus, the model was found to predict arcing levels for the cells under varying environmental and operational conditions and to allow data from one module to be accurately scaled to a module with different material and geometric parameters. This simulation could then be used to perform power system or solar cell design trade studies, with much less ground and flight testing needed for verification.

Nomenclature

A = Fowler–Nordheim coefficient $(1.54 \times 10^{-6} \times 10^{4.52\phi_W^{-1/2}}/\phi_W A/V^2)$
A_{array} = solar array area, m^2
A_{cell} = solar cell area, m^2
A_{wave} = discharge wave area, m^2
B = Flower–Nordheim coefficient $(6.53 \times 10^9 \phi_W^{1.5} V/m)$
b_n = coefficients in polynomial fit to d_i/d
C_{diele} = capacitance of dielectric, F/m^2
C_{front} = capacitance of coverglass front surface, F
C_s = ion acoustic velocity, m/s
C_1, C_2 = coefficients to arc rate fits
d = thickness of dielectric, m
d_i = distance of electron first impact point from triple junction, m
d_1 = thickness of coverglass, m
d_2 = thickness of adhesive, m
E_d = neutral adsorbate binding energy, eV
$E_{\max}$ = electron incident energy for maximum secondary electron yield, eV
E_{se} = secondary electron energy, eV
E_{se1} = electron incident energy for a secondary electron yield of unity, eV
e = electron charge
m_e = electron mass, kg
m_i = ion mass, kg
N_{cell} = number of solar cells in array
N_n = number density of neutral particles adsorbed on dielectric side surface, m^{-2}
N_{n0} = surface neutral density for monolayer coverage, m^{-2}
n_e = plasma number density, m^{-3}
n_{n_a} = ambient neutral density, m^{-3}
n_{nc} = critical desorbed neutral density for breakdown, m^{-3}
Q_{ESD} = effective electron stimulated desorption cross section, m^2
R = arc rate, s^{-1}
S_{FN} = emission site area determined from Fowler–Nordheim plot, m^2
S_{real} = emission site area determined by accounting for electron space charge effects, m^2
T_e = electron temperature, eV
T_i = ion temperature, eV
T_s = cell surface temperature, K
V_{arc} = voltage at which last arc occurred, V
V_{bias} = bias voltage of interconnector/conductor, V
V_e = voltage that minimizes arcing time, V
v_{ion} = mean speed of ions entering sheath, m/s
v_{orbit} = spacecraft orbital velocity, m/s
y = distance of emission site from the triple junction, m
α = angle of attack—angle between velocity vector and vector normal to array front surface
α_w = wake angle
β = field enhancement factor
γ_{ee} = secondary electron yield
$\gamma_{\max}$ = maximum secondary electron yield at normal incidence
Γ_{ESD} = electron stimulated desorption flux, /m^{2}s
Γ_i = ion flux onto array front surface, /m^{2}s
$\Gamma_{i_{\text{crit}}}$ = critical ion flux onto array front surface for arcing, /m^{2}s
Γ_n = neutral flux onto dielectric side surface, /m^{2}s
ΔQ = charge lost from coverglass by one discharge, C
ΔV = potential drop across dielectric due to arc discharge, V
ϵ_{d_1} = dielectric constant of coverglass
ϵ_{d_2} = dielectric constant of adhesive

Received Oct. 23, 1995; revision received June 29, 1996; accepted for publication Aug. 29, 1996.

*Research Assistant, Department of Aeronautics and Astronautics. Member AIAA.
†Professor, Department of Aeronautics and Astronautics. Associate Fellow AIAA.
‡Research Scientist, Geophysics Directorate.

η = factor accounting for difference in electric field at emission site and triple junction
θ_0 = Mach angle
κ = Boltzmann constant
ξ = factor accounting for difference of dielectric constants between coverglass and adhesive
ξ_0 = ξ at the coverglass front surface
τ_{arc} = time between arcs, s
τ_{chrg} = total charging time, $\tau_{ion} + \tau_{efee}$, s
τ_{efee} = enhanced field electron emission (EFEE) charging time, s
τ_{ion} = ion charging time, s
τ_{exp} = experiment time, s
ϕ_w = work function, eV

I. Introduction

PHOTOVOLTAIC power systems continue to be the most commonly used means of meeting power needs for both Department of Defense (DOD) and commercial satellites. In the past, most systems operated at low voltage levels, typically –28 V. Driven by higher power requirements, several modern spacecraft designs now utilize a somewhat higher bus voltage, with several satellites using −33 and −51 V bus voltages. Future space missions, however, will need still higher power than present systems, with power levels of 10 kW to 1 MW needed. To meet these requirements, the use of high current is undesirable for two reasons. First, high-current systems require more massive power distribution cables, increasing the mass of the spacecraft. Second, high current results in greater resistive losses during the power transmission. Thus, high voltage power generation and transmission at low currents is desirable. For example, the space station design calls for power to be provided by high-voltage solar cells operating at −160 V.

High-voltage solar arrays have been found to interact with the ambient space plasma environment in several manners, including current leakage,[1] arc discharges,[2] and enhanced drag due to Coulomb collisions.[3] For positively biased arrays, the current collection can become anomalously large, known as snap-over. This can result in a significant leakage power loss. For large negative voltages, arc discharges have been found to occur. An arc is typically defined as a sudden current pulse up to the order of an ampere on a time scale of a microsecond or less. The current pulse is often accompanied by a spot of light at the edge of the coverglass, which may interfere with optical systems.[4] Arcing can also result in electromagnetic interference (EMI) and solar cell damage, thus degrading the operation of both the power subsystem and the spacecraft as a whole. If the EMI generated by the arc couples to the spacecraft power system, it could become significant enough to disrupt communications between spacecraft, or between spacecraft and telerobotic systems.[4]

This paper will describe several previous experiments that have examined solar array arcing as well as several models that have been developed to explain the phenomenon. A detailed analysis of the data from the Photovoltaic Array Space Power (PASP) Plus experiment will then be presented, along with comparisons to model simulations.

A. Previous Experiments

Arcing on high-voltage solar arrays has been observed in both ground and space experiments. It was first observed in 1971 by Herron et al.[5] during plasma chamber tests of solar arrays biased between ±16 kV. Several ground tests examined the role of a dielectric on a conductor in arcing, confirming arcing on dielectric-conductor systems.[6–9]

In an experiment by Kuninaka,[10] luminosity was observed during arc discharges. This luminosity is believed to be due to collisions between electrons emitted from the conductor and neutral gas desorbed from the dielectric. The uv spectrum emitted during arcing was measured by Upschulte et al.[11] and was found to show a strong hydroxyl spectrum, indicating that water molecules are among those desorbed from the dielectric and ionized by the electron current. The duration of an arc is typically assumed to be on the order of a microsecond, based on several experiments.[11–13] Several ground experiments measured the effect of operational, environmental, and geometric parameters on the arc rate. Experiments by Kuninaka[7] and Hastings et al.[14] found that the arc rate increases with voltage and plasma density and decreases with temperature. Experiments by Grier[15] and Miller[6] also found an increase in arc rates with increasing voltage, and Miller's tests also found increasing arc rate with plasma density. Upschulte et al.[11] observed that overhanging the coverglass 10–20 μm over the adhesive substantially lowers the arc rate. To reduce arcing on solar arrays, a new cell design was created, known as the wrap-through-contact cell. In this design, the metal interconnects are not exposed to the ambient plasma. Instead, the interconnects run underneath the coverglass, down through a hole in the center of the cell, and then under a kapton substrate to the adjacent cell. However, the semiconductor is still exposed to the plasma, leading to a possible arcing site.[16] Leung[12] found that wrap-through-contact cells did arc, although less frequently than conventional geometry cells.

The occurrence of arcing on conventional geometry solar cells in the space environment was verified by the two Plasma Interactions Experiments (PIX I and II) in 1978 and 1983,[15,17,18] where arcing was observed at voltages as low as −255 V. Arcing on both conventional and wrap-through-contact cells was later observed on the NASA Solar Array Module Plasma Interactions Experiment (SAMPIE), conducted aboard the Space Shuttle in March 1994 (Ref. 19).

B. Arcing Onset Model

Using numerical and analytic methods, Cho[20] developed a model to describe the arc initiation process, which is the model used in this work. In this model, the arc location is at the triple junction of the plasma, interconnect, and dielectric layer (i.e., coverglass and adhesive). The arcing mechanism is described in detail in Refs. 14 and 20–22 and can be summarized as follows. Ambient ions charge the dielectric (i.e., coverglass and adhesive) front surface but leave the dielectric side surface uncharged. This creates a strong electric field at the conductor surface, inducing prebreakdown electron emission due to enhanced field electron emission (EFEE). Some of the emitted electrons strike the dielectric side surface, inducing the release of secondary electrons and causing electron stimulated desorption of neutrals adsorbed on the dielectric surface. The secondary electron emission further charges the dielectric and increases the electric field, providing a positive feedback mechanism. This leads to EFEE runaway and possible ionization of the desorbed neutral gas. A discharge wave created by the arc resets the charging process at all of the emission sites within the area covered by the wave.

This model was produced through the use of computer particle-in-cell (PIC) and Monte Carlo simulations of the arc initiation process. These results were then used to develop analytical formulas for the ion charging time and the EFEE charging time. The total charging time at an emission site is the sum of the ion charging time and the EFEE charging time given by

$$\tau_{chrg} = \frac{\{V_e - [V_{arc} - (\Delta Q/C_{front})]\}C_{front}}{en_e v_{ion} A_{cell}} + \frac{C_{diele} d_i^2}{(\gamma_{ee} - 1)\sqrt{S_{real}}\eta\xi A(S_{FN}/S_{real})B\beta} \exp\left(\frac{Bd}{\beta\eta\xi_0 V_e}\right) \quad (1)$$

Once EFEE runaway has occurred, it was found that breakdown[20] would occur if the desorbed neutral density was greater than a critical density of approximately 6×10^{21} m^{-3}. The desorbed neutral density is given by

$$n_n = 2.08 \frac{N_n Q_{ESD}}{\bar{c}} \frac{\epsilon_0}{e} \sqrt{\frac{2e}{m_e}} \frac{\sqrt{E_{se}}}{E_{se1} d^2} V_e^2 \quad (2)$$

where the adsorbed neutral density on the dielectric surface before the intensive outgassing due to the EFEE begins is given as a function of time since the last arc at that location by

$$N_n(t) = (A_1/A_2)(1 - e^{-A_2 t}) \quad (3)$$

where A_1 and A_2 are given by

$$A_1 = n_{na} v_{\text{orbit}} \sin\alpha + n_{na}(\bar{c}/4)$$
$$A_2 = \left(C_1 / N_{n_0}\right) + k_1^0 \exp(-E_D/\kappa T_s) \tag{4}$$

A semianalytic computer code was then developed to predict the arc rates for high-voltage solar arrays placed in a plasma environment.[20,21] In this model the cell temperature is a critical factor in the arcing process, since the density of neutrals adsorbed on the dielectric side surface is a strong function of the cell temperature. These neutrals are then desorbed and ionized, producing the arc discharge.

Two other models have been proposed to explain the arcing process. The first, proposed by Parks et al.,[23] based on previous work by Jongeward et al.,[24] attributes the arcing onset to the Malter effect at a thin dielectric layer on the conductor surface. The second model, by Thiemann and Schunk,[25] proposes that arcing occurs at the cell side surface, due to secondary electron emission runaway on the Kapton substrate. Note that in neither of these two models should the cell temperature greatly affect the arcing process, which was seen in the ground experiments by Kuninaka.[7]

C. Overview of this Paper

In this paper, the semianalytic model was used to predict the arcing rates for the conventional geometry cells on the PASP Plus diagnostics experiment. This Air Force experiment was flown to examine the interactions between high-voltage solar arrays and the ambient space plasma and radiation environments. In the next section, the PASP Plus experiment will be described, and then the results of the simulations will be discussed. The data from the experiment will then be analyzed to examine correlations between arc rates and the cell properties, environmental variables, and operational parameters and to verify the accuracy of the model.

II. Description of PASP Plus

The interactions between solar arrays and the ambient plasma and radiation environments need to be properly understood to design power systems that will survive and perform as desired. Because of the complex nature of these interactions, ground simulations are often inadequate to accurately quantify the effects of the space environment on the solar array systems. Thus, the PASP Plus experiment was designed by the U.S. Air Force to gather a large base of flight test data to be used to develop an understanding of the interaction of both highly positive and negative biased solar arrays with the space environment. The experiment was designed to systematically investigate the effects of the space environment on advanced solar arrays. The PASP Plus experiment is the primary experiment on the advanced photovoltaic and electronics experiment (APEX) satellite.

On Aug. 3, 1994, the APEX satellite was launched into orbit by a three-stage solid-fuel Pegasus rocket released from the NASA B-52 aircraft within the Western Test Range off of the coast of California. The launch occurred without problems, as did the satellite's lock onto the sun and the deployment of the four panels. The satellite was placed into a 70-deg inclination, 363 × 2550 km orbit, which has an apogee higher than the baselined 1950-km apogee. This higher altitude allows the satellite to traverse farther into the radiation belts, allowing the radiation effects portion of the experiment to be performed in roughly half of the time originally needed.[26]

A. APEX Satellite

The deployed configuration of the APEX satellite is shown in Fig. 1. The body of the satellite is a hexagonal cylinder 152 cm tall and 96.5 cm across. The top payload shelf contains eight solar array modules, three electric field transient pulse monitors, the APEX sun sensor, one calorimeter, and two quartz crystal microbalances. Extending up from the payload shelf are two 60-cm booms. On one boom is the Langmuir probe head, and on the other is the APEX magnetometer, which is used for satellite attitude control. Under the payload shelf is the avionics shelf, which contains electronics boxes and the other secondary experiments. The satellite has four deployed panels attached to the top shelf. Three of these panels contain the solar arrays used for spacecraft power, while the fourth deployed panel contains the remaining PASP Plus solar array modules and diagnostic sensors. There is one transient pulse monitor (TPM), one calorimeter, one quartz crystal microbalance (QCM), and the PASP Plus sun sensor on the panel. The satellite is three-axis stabilized and is sun pointing to within ±0.5 deg. Thus, the solar arrays are at varying angles of attack to the ram plasma flux as the satellite moves around its orbit. Because the Langmuir probe head is 60 cm away from the shelf, the plasma density recorded by the probe while the array modules are in wake does not match that at the location of the modules.[26]

B. Diagnostic Equipment Description

The PASP Plus experiment is controlled by a microprocessor controller, which contains all of the electronics for the solar cell biasing

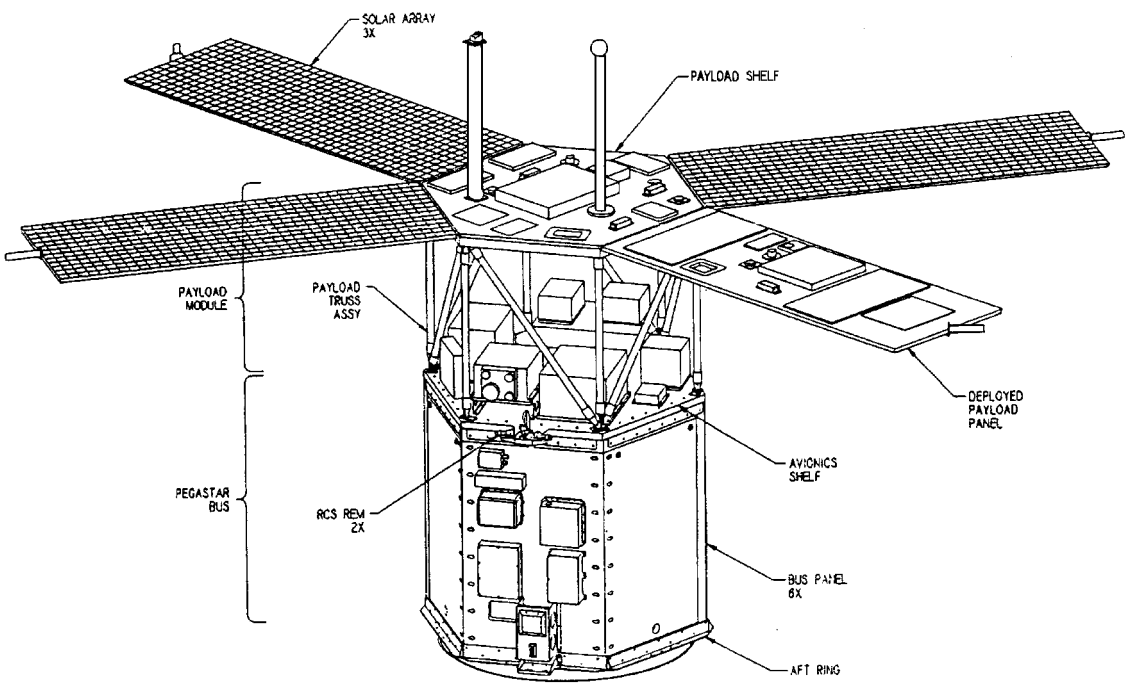

Fig. 1 Deployed Apex spacecraft with PASP Plus experiment.

and data acquisition and telemetry. The controller distributes power and commands from APEX to all of the instruments, except for the dosimeter, and receives, processes, and sends the data from the instruments to the satellite. The data are then stored for later transmission to a ground station or sent down in real time. The dosimeter has its own interface for power, command, and data transmission to and from the satellite.[26]

Diagnostic sensors for the PASP Plus experiment include[26] the following.

1) A sun sensor to measure the incident angle of the solar energy.

2) A Langmuir probe to measure the plasma temperature and density. The probe also has a potential sensor (SENPOT) to sense and compensate for the vehicle frame potential, which may be more negative than the space plasma potential. The Langmuir probe can measure plasma densities of 10^8 to 10^{12} m^{-3} and plasma temperatures of 1000 to 8000 K, with debye lengths of 2.2 mm to 62 cm, at spacecraft potentials of 2 to -30 V (Ref. 27).

3) Four TPMs to detect and fully characterize (amplitude, rise time, integral, and number of pulses per second) the arc discharges that occur during the negative biasing portion of the experiment.[28] These monitors have a rate limitation of 15 arcs per second. There is also one sensor on the high-voltage power line inside the controller. The minimum electric field pulse counted by the TPMs can be chosen from preset levels, listed in Table 1.

4) An electrostatic analyzer (ESA) to measure the 30 eV to 30 keV electron/ion spectra and to detect the passage of the spacecraft through the auroral region. The ESA has four heads: two for ions and two for electrons. The instrument can measure one ion and electron spectrum per second, with an energy resolution of 10%. The number flux range measurable is 10^5 to 10^{10}/cm$^2\cdot$ s $\cdot$ sr, integrated, at integrated energy fluxes of 10^5 to 10^{10} keV/cm$^2\cdot$ s $\cdot$ sr (Ref. 27).

5) A dosimeter to measure the short- and long-term ionizing particle (electron and ion) radiation flux and dosage.

6) Contamination monitors to measure the amount and effect of molecular and particulate contamination on the array surfaces. Two types of monitors will be used. QCMs will be used to measure the mass of contamination being deposited on the surface, while thermal coated calorimeters will determine the optical degradation of the coverglass through α/ϵ measurements.

(7) Temperature sensors to measure the temperature of the arrays.

In addition, an electron emitter will be available to emit a stream of electrons to alter the spacecraft potential. This will allow the experiment to more accurately simulate the positive bias voltage operation of large functional arrays.

Table 1 PASP Plus TPM settings

Setting	Telemetry counts	E-field threshold, V/m	In-line sensor threshold, mA
0	5	10	6
1	55	45	30
2	105	225	140
3	155	700	420

C. Solar Array Module Descriptions

There are 17 arrays of 12 different types being flown on the payload shelf and deployed panel of the spacecraft. Since there are only 16 electrical channels, 1 of the arrays is not being used. Ten of these arrays are subject to high-voltage biasing. The information for these arrays is taken from Refs. 29 and 30. The array modules are numbered from 0 to 15 for identification. Figure 2 shows the location of each module on the payload shelf and deployed panel. The number in parentheses beside the array name is the number of cells in the module. Arrays 0, 1, and 2 are conventional silicon solar cells. These cells have a dielectric thickness of 190 μm. Module 3 is made up of silicon wrap-through-contact (WTC) cells designed for the space station. Arrays 4 and 6 are Applied Solar Energy Corporation's (ASEC) gallium arsenide/germanium (GaAs/Ge) conventional cells, with a dielectric thickness of 153 μm. TRW's Advanced Photovoltaic Solar Array (APSA) cells make up array 5 (previously labeled array 36) and have a dielectric thickness of 127 μm. The advanced solar cells of AlGaAs/GaAs monolithic multiband gap (MBG) are on array 7. Array 8 is made of Spectrolab's GaAs/Ge WTC cells. Amorphous silicon cells developed by TRW and Solarex are located in module 9. Array 10 contains advanced indium phosphate (InP) cells. Spectrolab's conventional GaAs/Ge cells are in array 11, with a dielectric thickness of 22 μm. Modules 12 and 13 are made up of Boeing's GaAs/CuInSe MBG cells. Two concentrator designs are being flown in modules 14 and 15. Module 14 is the Mini-Cassegrainian GaAs cell from TRW, while module 15 contains the Boeing Mini-Dome Fresnel Concentrator. Of these, modules 1–6, 8, 11, 14, and 15 are the arrays subject to high-voltage biasing. The arc rate simulation was run for the conventional geometry cells (arrays 1, 2, 4–6, and 11). The geometric and material properties of the conventional and WTC modules are listed in Table 2.

D. Experiment Operation

After the turn-on and checkout of the APEX spacecraft in orbit and initial current-voltage (I-V) curve measurements, PASP Plus experimental operations began on Aug. 8, 1994, with positive biasing of the solar array modules. In both the positive and negative biasing, each array to be tested is biased in a sequence of four steps each lasting 23 s, with each step preceded by an I-V curve measurement on the module being tested, an I-V curve of one of the other 16 modules, and a Langmuir probe measurement of the plasma density and temperature.[27] The modules to be tested are biased in descending numerical order using the four-step bias sequence. The biased arrays can be either shorted or at optimum load, with bias voltages between +500 and -500 V possible. The other mode of experimental operation is the I-V curves only mode, which produces one I-V curve for each of the modules in 8 min.

Negative biasing of the modules to be tested began on Aug. 22, 1994 (day 94,234). This phase continued until Sept. 3, 1994 (day 94,246), with biasing from -75 to -450 V being done on all arrays except 5, which was biased up to -300 V. The biasing up to -220 V (days 94,234–94,237) was done within $\pm$20 min of perigee. At this point, high levels of arcing were seen, especially on the APSA module 5 while in eclipse when the cells were cold.[31] Because of

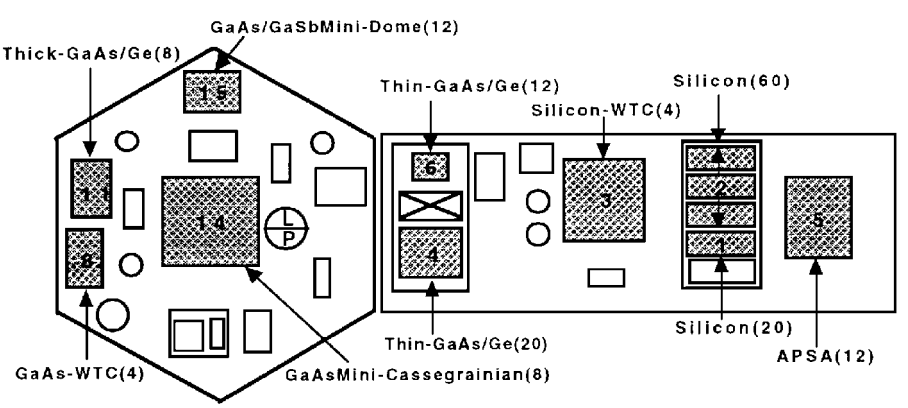

Fig. 2 PASP Plus solar array module locations.

Table 2 PASP Plus cell data

	Module no.					
	1, 2	3	4, 6	8	11	5 (36)
Cell type	Si	Si WTC	GaAs/Ge	GaAs/Ge WTC	GaAs/Ge	APSA
Manufacturer	RCA	NASA	ASEC	Spectrolab	Spectrolab	TRW
Cell size, cm^2	2×4	8×8	4×4	4×4	4×4	2.6×5.1
No. of cells	20, 60	4	20, 12	4	8	12
Cell gap, μm	500	1000	500	1000	500	635
d_{cell}, μm	203	203	89	178	178	56
d_1, μm	153	203	102	152	152	51
d_2, μm	37	N/A	51	N/A	76	76
ϵ_{d_1}	3.5	4	4	4	4	4
ϵ_{d_2}	2.7	3	2.7	3	2.7	2.7
γ_{max_1}	3.46	4	4	4	4	4
γ_{max_2}	3	2	3	2	3	3
E_{max_1}, eV	330	400	400	400	400	400
E_{max_2}, eV	300	200	300	200	300	300
ϕ_w, eV	4.76	4.85	4.26	4.5	4.26	4.26

concerns over damaging the PASP Plus experiment in this early phase, the decision was made to continue negative biasing from only 15 min after exiting penumbra to 1 min prior to entering penumbra.[31] Thus, the negative biasing from −240 to −450 V (days 94,240–94,246) was conducted only in sunlight, when the cells were hot. Upon biasing at −450 V, the TPMs became saturated. It was decided that this was due to fluctuations in the power supply and not arcing, and therefore biasing was continued only up to −430 V (Ref. 31).

Biasing from −160 to −400 V was next carried out Oct. 17–22, 1994 (days 94,290–94,295). The APEX orbit during this time was in a noneclipse orientation, and so the cells were always hot when biased, gathering a large number of data points at the high temperatures. Because arcing data were desired during eclipse times, positive biasing was resumed Oct. 24–30, 1994, while the satellite remained in a sunlight-only orbit. Negative biasing was then continued from Oct. 31–Nov. 4, 1994 (days 94,304–94,308), when the APEX orbit contained portions of eclipse. The bias voltages in this portion of the experiment were predominantly from −160 to −300 V, with a few points from −310 to −370 V. On Nov. 4, 1994, as the negative biasing beyond −300 V was being conducted, a problem developed on APEX, causing the spacecraft to go into contingency mode and to shut off the experiments. The problem that developed was in the battery control regulator. Software to work around the problem was written and tested and then uploaded to the spacecraft, allowing experimental operations to resume on Jan. 14, 1995.

With PASP Plus once again operational, positive biasing was conducted Jan. 14–17, 1995, and negative biasing from Jan. 18–Feb. 11, 1995 (days 95,018–95,042). Because of high levels of noise in the TPM data,[31] the TPM threshold was increased from level 0 to 1 on Feb. 2, 1995 (day 95,033). The counts detected on these days are believed to be noise (not arcs) for several reasons. First, the counts are an order of magnitude higher than the previous data and are independent of which cell is biased or what bias voltage is used. Also, although the counts show up, there is no amplitude measured, indicating low-level noise and not arcing.

Because of the high noise in the data for days 95,018–95,032, these data will not be used in this paper. On days 95,033–95,042, the arrays were biased between −240 and −440 V. In this set, one module was biased repeatedly for four consecutive orbits, then the next module was biased for four orbits, etc. This was done to try to get data at continuous points in the cell temperature and plasma density ranges seen throughout the orbit.

The next phase of negative biasing was performed from March 3–April 1, 1995 (days 95,062–95,091), when there were portions of the eclipse that had the modules in ram. The same scheme was used as in the last phase: biasing one array at a time repeatedly for several orbits, then moving on the next array to be tested. The last set of negative biasing to be discussed in this paper took place from April 13–18, 1995 (days 95,103–95,108). Reference 21 contains a more complete discussion of the PASP Plus experiment and lists the exact bias sequencing used on each day of negative biasing.

E. Flight Data Processing

The raw data from the satellite were first processed by software written by Boston University[32] and then distributed to the PASP Plus science team. These data include the satellite housekeeping and ephemeris data, environmental data, and the positive and negative biasing data. The data were then analyzed by examining the variation of arc rate with one parameter while keeping the remaining parameters constant. The appropriate data points were found by choosing which parameters to hold constant at given values and then scanning the data set to find the corresponding arcing data points. When the data were averaged, error bars were set to standard deviations determined using Gaussian statistics if there were more than one point at each value of the independent variable; otherwise, Poisson statistics were used.[18] On graphs showing the actual flight data points (not averages), discrete levels of arc rates are seen because the arc rate is calculated from the discrete pulse counts divided by the constant experiment duration.

III. Arc Rate Simulations

The arc rate simulation[20,21] was run both pre- and postflight for the conventional geometry solar cell modules on PASP Plus. The preflight simulations were conducted using environmental parameter values generated using the Environmental Workbench (EWB) software from S-cubed,[33] assuming the 360×1950 km, 70-deg baseline orbit. The EWB software provides a user interface to the standard neutral, plasma, and radiation environmental models. The arc rate simulations showed a fair agreement with the flight data, although the cell temperatures used in the simulations were between 30 and 50 K colder than the actual flight conditions.

The simulations were then rerun postflight as soon as the initial negative biasing data were processed, using the environmental parameters and cell temperatures measured during the experiment, where available, listed in Table 3. The EWB generated values of ion mass, neutral density, and neutral temperatures were again used, because they were not measured during the experiment. A maximum plasma density of 3.5×10^{11} m^{-3} was used, because the experimental Langmuir probe data above 2×10^{11} m^{-3} was unreliable. The cell temperatures used are given in Table 4, which are the ranges seen during the first day of negative biasing (day 94,234). The maximum temperature corresponds to the minimum arcing condition and vice versa. In eclipse, the APSA array was coldest at 205 K, whereas the remaining cells ranged from 231 to 255 K. The standard silicon cells were coolest in sunlight, at 311 K, whereas the remaining modules ranged from 323 to 333 K. Figure 3 shows the mean values of the postflight simulations for the silicon module 1 at the maximum temperatures in Table 4. The neutral density for the maximum arcing condition in these simulations was 3.18×10^{14} m^{-3}, which is the maximum density from the EWB generated environmental data for the APEX orbit. At lower neutral densities, lower arcing would be expected at the higher cell temperatures. Also shown in the graph are the flight data points with temperatures four degrees colder than the temperature in the simulations, ±3%,

Table 3 Postflight environmental parameters for minimum/maximum arcing

Condition	Plasma density, m^{-3}	Electron temp., eV	Ion mass, kg	Orbital velocity, m/s	Neutral density, m^{-3}
Minimum	$1. \times 10^{8}$	0.023	2.64×10^{-26}	6195	6.85×10^{9}
Maximum	3.5×10^{11}	0.85	2.21×10^{-27}	8211	3.18×10^{14}

Table 4 Temperature ranges of biased PASP Plus conventional cells

Module no.	1	2	4	5	6	11
Minimum, K	231	231	255	205	255	253
Maximum, K	311	311	329	333	329	323

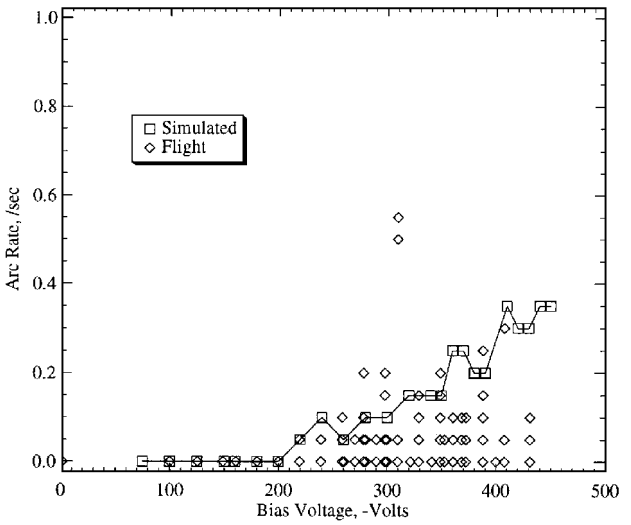

Fig. 3 Postflight simulations and flight data for silicon module 1 at T_S = 307 K.

because there are very few data points at the temperature extremes themselves. Figure 4 shows the mean values of the postflight simulations using the minimum temperatures from PASP Plus in Table 4, along with flight data points 4 K warmer than the temperature in the simulations, ±3%. In both cases, the mean value of the simulations agrees with the general trend of the arcing activity. There is observed to be a threshold at about −200 V followed by a nonlinear increase in the arcing as a function of voltage. The wide variation in the data stems both from the statistical nature of the arc process and the variation with the orbital parameters. Since not all of these are known, exact agreement with the experimental data is impossible to attain. However, approximately 99% of the flight data fell within the range predicted by the simulations. Also, the high arc rate data points measured between −260 and −300 V all occurred before the TPM threshold was increased, suggesting that these may have been due to low-level noise other than arcing. In general, similar agreement was found for the other conventional geometry cells. The thin GaAs/Ge modules showed less arcing than expected, however. This could possibly be due to a lower emission site density, to which the arcing rate is very sensitive. Also, the arcing levels at the high temperatures are more difficult to predict, because at these temperatures the arcing becomes very sensitive to the unknown parameters such as neutral density and the desorption yield. Thus, it was found that, given the correct environmental parameters, the model simulation was able to predict the arcing rates for the PASP Plus experiment. The model simulation can then be used to predict the arcing activity on any conventional geometry solar array under any given set of environmental and operational parameters.

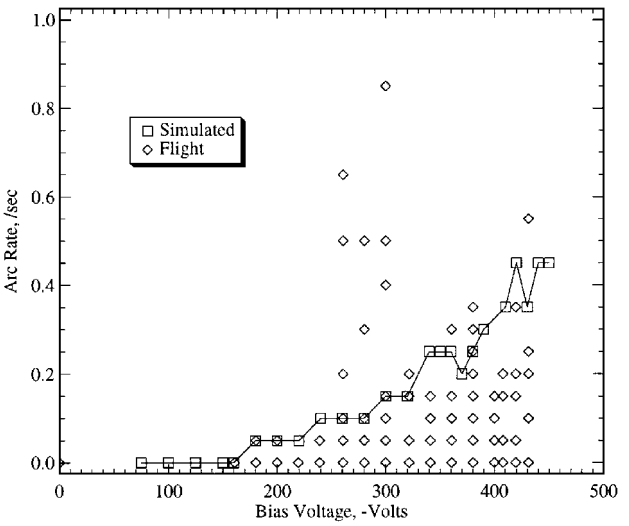

Fig. 4 Postflight simulations and flight data for silicon module 1 at T_S = 249 K.

IV. Flight Data Analysis

In this section, the PASP Plus flight data will be examined to determine correlations between the arcing rates of the various modules with the environmental variables, operational parameters, and cell properties that are known for the experiment. From the model used in this work, the arc rate is expected to be a function of bias voltage, array area, dielectric thickness, ion flux, neutral flux, and surface temperature, as well as the various EFEE parameters. Thus, the arc rate can be expressed as $R = R(V_{\text{bias}}, A_{\text{array}}, d, \Gamma_i, \Gamma_n, T_s, \text{EFEE})$. Correlations with these parameters will be examined, as well as possible dependencies on radiation flux, ram angle (which affects the ion flux), and transition into and out of eclipse.

A. Arc Rate Dependency on Bias Voltage

The arc rate of solar arrays biased to high negative voltages is given by the inverse of the charging time, given by Eq. (1), times the ratio of array area to discharge wave area. The arc rate expected for an array can then be given by

$$R = \frac{A_{\text{array}}/A_{\text{wave}}}{(\{V_e - [V_{\text{arc}} - (\Delta Q/C_{\text{front}})]C_{\text{front}}\}/en_e v_{\text{ion}} A_{\text{cell}} \cos\alpha) + \left[C_{\text{diele}} d_i^2 \Big/ (\gamma_{ee} - 1)\sqrt{S_{\text{real}}}\eta\xi A(S_{FN}/S_{\text{real}})B\beta\right]\exp(Bd/\beta\eta\xi_0 V_e)} \tag{5}$$

Thus, setting all parameters except the bias voltage constant, and assuming that the potential across the coverglass drops by a constant fraction of the bias voltage, the premultiplier of the EFEE term is constant, and V_e is a constant fraction of V_{bias}, the arc rate can be written as

$$R = \frac{1}{C_0 V_{\text{bias}} + C_1 \exp(C_2/V_{\text{bias}})} \tag{6}$$

At low bias voltages, the EFEE term will dominate the charging process and the ion charging term can be neglected, further simplifying the equation for arc rate to

$$R = \frac{1}{C_1 \exp(C_2/V_{\text{bias}})} \tag{7}$$

Figure 5 shows the variation in average arc rate with bias voltage for the silicon module 2 for days 95,033–95,108 at an ion flux of $1 \times 10^{13}/\text{m}^2\text{s}$ and cell temperature of 245 K. The error bars show one standard deviation from the average at each voltage. There is clearly a strong dependence of arcing on bias voltage. The curve shows a fit to the data made using the form given by Eq. (7). Although the shape of this form fits the data well and models the onset characteristics

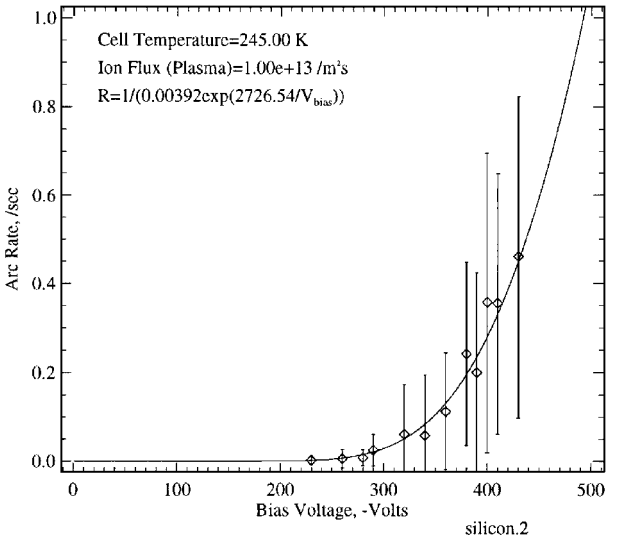

Fig. 5 Arc rate variation with bias voltage for silicon module 2.

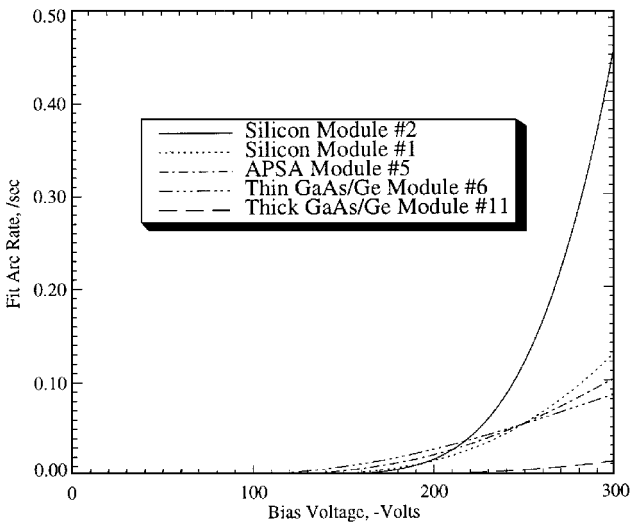

Fig. 6 Arc rate fit to bias voltage for conventional geometry cells.

accurately, the coefficients do not match those expected from the model. This is because in performing a fit all other parameters are assumed to be constant. This, however, is not the case, because parameters such as the enhancement factor are seen to vary greatly with bias voltage in the simulations. Similar results were found for all of the conventional geometry cells. The WTC cells also exhibited arcing, although much less frequently than the conventional cells. The two concentrator modules showed very little arcing, such that it was difficult to distinguish possible arcs from noise. Figure 6 shows a comparison of fits made for all of the conventional geometry cells on days 94,234–94,308 at eclipse temperatures and an ion flux of $1 \times 10^{14}/\mathrm{m}^2\mathrm{s}$, except module 4, which did not have enough points available for a fit to be made. Because of the large number of data points, plotting the data for all of the cells on the same graph would make any cross-cell comparisons impossible. By plotting just the fits to the data on one graph, arcing levels from various cell types can be compared. This shows that the silicon and APSA cells showed the highest arcing, and the thick GaAs/Ge module had very low levels of arcing.

1. Onset Voltage

At high ion fluxes, the total charging time will be dominated by the EFEE charging time, and the arc rate can be given by Eq. (7). The EFEE charging time will then determine the threshold voltage at which arcing will begin. The charging time, as a function of bias voltage, is given by the form

$$\tau_{\mathrm{chrg}} = C_1 \exp(C_2/V_{\mathrm{bias}}) \tag{8}$$

Table 5 Simulated and experimental arcing onset voltages

Array	Simulated onset voltage, V	Experimental onset voltage, V
(1, 2) standard silicon	−160	−160
(3) silicon WTC	N/A	−160
(5) APSA	−100	−75 to −125
(4, 6) thin GaAs/Ge	−120	−125
(8) GaAs/Ge WTC	N/A	−260 to −300
(11) thick GaAs/Ge	−180	−180

For any finite experiment duration, there will exist a voltage below which the charging time exceeds the experiment duration, at which point no arcing will be seen. This voltage is the arcing onset voltage for the array at the given experiment time. Onset voltages were found using both the flight data and the simulations, which are summarized in Table 5. Because the simulation used in this work is based on a model of arcing on conventional geometry cells, simulated onset voltages could be found only for the conventional geometry cells on PASP Plus. To find onset voltages in the simulations, a cell temperature of 200 K, an ion flux of $3.5 \times 10^{11}/\mathrm{m}^2\mathrm{s}$, and an experiment duration of 60 min were used as extreme values. In the flight data, the onset voltage was taken to be the voltage below which arcing did not occur, which requires a judgment to be made as to whether a single pulse is an arc or some other noise. The very low arcing activity on the concentrator arrays makes determining an onset voltage problematical. As seen from the table, the simulations predict the onset voltages very accurately. The onset voltages observed during the experiment are a significant finding by the PASP Plus experiment, because previously it was believed by the space power community that solar arrays could be operated up to −300 V before arcing would become a concern.[34] This experiment has shown that arcing may be an issue at much lower voltages, which are at the level of current designs for the space station.

2. Area Scaling

From Eq. (5), it can be seen that, all else being equal, the arc rate is expected to scale linearly with array area. Thus, it would be expected that module 1 would have an arc rate one-third that of module 2. If the arc rate for an array of area A_i is fit using Eq. (7), the scaled rate for a similar array of area A_j would be given by[21]

$$R_j = \frac{A_j}{A_i} R_i = \frac{A_j}{A_i} \frac{1}{C_{1_i} \exp\left(C_{2_i}/V_{\mathrm{bias}}\right)} \tag{9}$$

Figure 5 shows the fit to the arc rate of the silicon module 2, which results in coefficients of $C_1 = 0.002677$ and $C_2 = 2011.77$. The scaled equation for silicon module 1 is then

$$R_1 = \frac{160\,\mathrm{cm}^2}{480\,\mathrm{cm}^2} \frac{1}{[(0.002677 \exp(2011.77/V_{\mathrm{bias}})]}$$

$$= \frac{1}{0.008031 \exp(2011.77/V_{\mathrm{bias}})} \tag{10}$$

Figure 7 shows the fit to the arc rate data of silicon module 1, along with the scaled fit from Eq. (10). The solid line is the fit to the data for module 1, whereas the dashed line shows the scaled curve from module 2 given by Eq. (10). Both curves are seen to fit the data equally well. A similar scaling was conducted on the two thin GaAs/Ge arrays (modules 4 and 6), which had an area ratio of 20 to 12. Again, the scaled curve fit the data as well as the curve found by fitting the data directly. These results support the linear area scaling suggested by the model. Thus, once the arc rate is known for a given solar array, the expected rate for a similar array of different size can be determined from a simple area ratio scaling.

3. Dielectric Thickness Scaling

The thickness of the solar array dielectric layer (i.e., coverglass and adhesive) is expected to be a key parameter in determining the arc rate. As the dielectric thickness is increased, the arcing rate is expected to decrease, because it is this thickness that determines

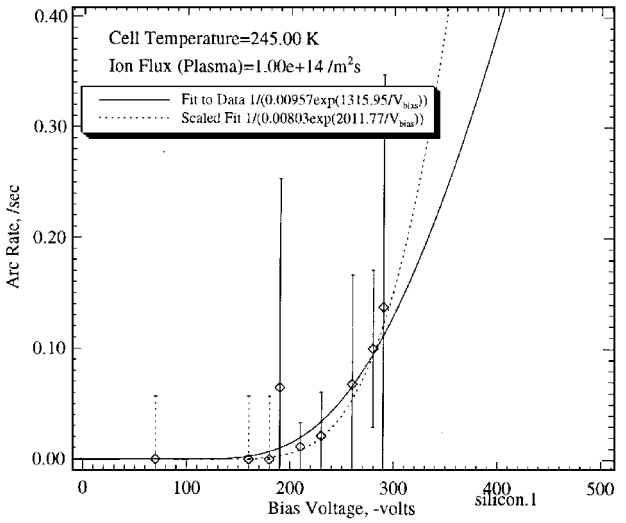

Fig. 7 Area scaling on silicon module 1.

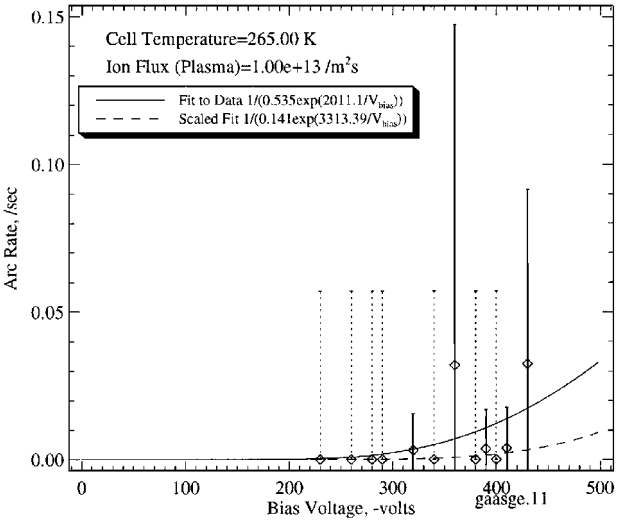

Fig. 8 Dielectric thickness scaling on GaAs/Ge module 11.

the strength of the electric field in the region of the triple junction ($E = -\phi/d$). However, a thicker dielectric also results in an increased mass. Thus, there exists a tradeoff between an acceptable level of arcing and solar cell mass. The coefficients in Eq. (7) are both functions of the dielectric thickness. The coefficients for a cell of dielectric thickness D_1 can be scaled to a cell of thickness D_2 by[21]

$$C_{1_2} = \frac{D_1 \sum_n b_n (y/D_1)^{1/2n}}{D_2 \sum_n b_n (y/D_2)^{1/2n}} C_{1_1} \qquad C_{2_2} = \frac{D_2}{D_1} C_{2_1} \qquad (11)$$

where b_n are the coefficients to a polynomial fit to the numerically determined electron first impact location. This scaling, however, assumes that the other parameters in Eq. (5) remain constant between the two cells. Unfortunately, this is not necessarily the case. In particular, the average value of the enhancement factor β of the emission sites that arc can vary between cells. Since this parameter appears within the exponential term, it will strongly affect the arcing rate and must be accounted for to scale between cells of differing dielectric thickness. Numerical studies of the thin and thick GaAs/Ge cells found that the average enhancement factor decreases with bias voltage for both arrays, and the average enhancement factor on the thick cell is approximately 1.25 times that of the thin cell.[21] Thus, the coefficients C_1 and C_2 can be scaled by this factor, β_f, to take into account the difference in the enhancement factor between the two cells.

A fit using Eq. (7) for the thin GaAs/Ge module 4 yielded coefficients of $C_1 = 0.0628$ and $C_2 = 2779.69$. Scaling these coefficients using Eqs. (9) and (11) and adjusting for the variation in the field enhancement factor yields coefficients for the thick GaAs/Ge module 11 of $C_1 = 0.141$ and $C_2 = 3313.39$. Figure 8 shows a comparison of the scaled fit and the fit to the data itself for the thick cell. The scaled fit is somewhat lower than the fit to the data but is still within the error bars and is a reasonable fit considering the variation seen in the arc rate at the different voltages. The large scatter in this data set makes the results somewhat inconclusive, but the dielectric scaling does appear valid. Unfortunately, to perform this scaling, the simulation must be run to determine the relationship between the average β values for the cells being examined. Once this relationship is known, experimental data from a cell of one dielectric thickness can be scaled to predict arcing rates for a similar array with a different dielectric thickness. Thus, the trade between arcing and mass can be conducted either using the simulation itself to predict arcing rates or by measuring arcing on one cell and then scaling for varying dielectric thicknesses.

4. Work Function Scaling

The work function of the interconnector determines the magnitude of EFEE. Thus, cells with a lower work function will exhibit higher electron emission and, thus, have a higher arc rate. The

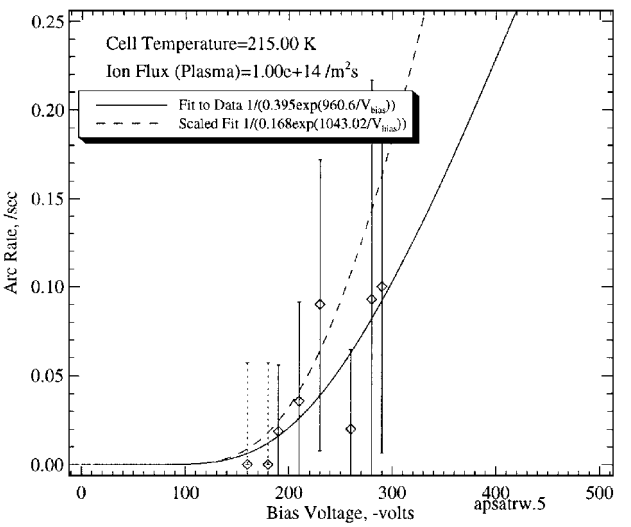

Fig. 9 Dielectric thickness, area, and work function scaling on APSA module 5 (days 94,234–94,308).

coefficients from the fit using Eq. (7) can be scaled for cells with a different work function by[21]

$$C_{1_2} = 10^{(4.52/\sqrt{\phi_{w_2}} - 4.52/\sqrt{\phi_{w_1}})} \sqrt{\left(\phi_{w_2}/\phi_{w_1}\right)} C_{1_1}$$
$$C_{2_2} = \left(\phi_{w_2}/\phi_{w_1}\right)^{1.5} C_{2_1} \qquad (12)$$

Because no two modules on PASP Plus differ only in work function, this scaling cannot be tested independently. Instead, this scaling, along with the area and dielectric thickness scalings, were applied to scale the silicon module 1 fit to the APSA module 5 data. The cell properties for these modules are listed in Table 2. As well as having different thicknesses and work functions, these cells also have different dielectric constants and secondary electron yield characteristics. Also, as noted previously, the silicon cells are believed to have a higher emission site density, which would result in a different β variation between the two modules than was determined from the simulations. Thus, the scaling, which assumes that these properties are the same, can be expected to yield a scaled fit that is higher than the actual fit to the data. Applying the scalings from Eqs. (9), (11), and (12) to the coefficients from the fit shown in Fig. 7 yields coefficients for the APSA module of $C_1 = 0.168$ and $C_2 = 1043.02$. In performing these scalings, a value of 1.4 was used for β_f based on the simulation results. Figure 9 shows the scaled curve, along with the fit to the data itself. The scaled curve (shown as a dashed line) is

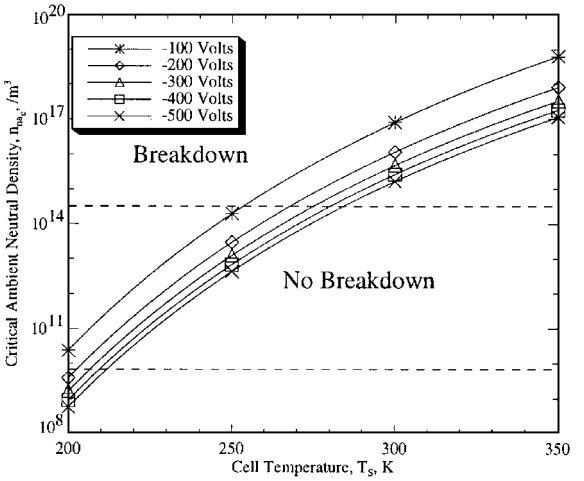

Fig. 10 Expected critical ambient neutral density variation with temperature for varying bias voltages for the APSA module 5.

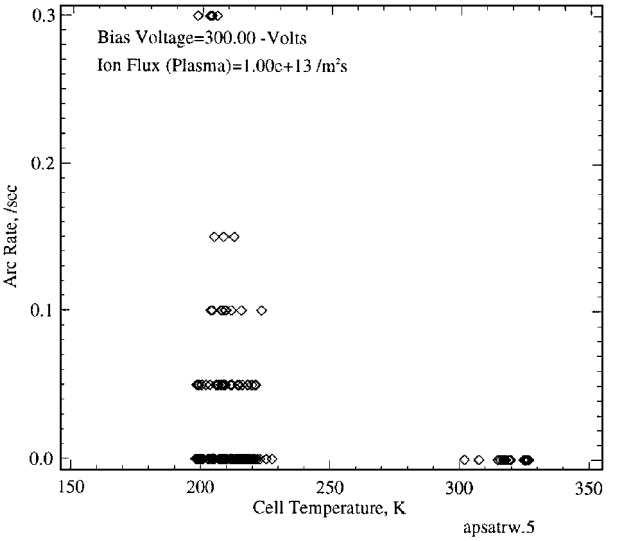

Fig. 11 Arc rate variation with cell temperature on APSA module 5 at −300 V and 1 × 10^{13}/m^{2}s ion flux (days 95,033–95,108).

somewhat higher than the fit, as expected, but still reasonably represents the arcing activity. Thus, all of the scalings can be applied to the results of testing a single module to estimate the arcing rates on arrays with different areas, dielectric thicknesses, and interconnect work functions.

B. Arc Rate Dependency on Cell Temperature

As discussed previously, the cell temperature is a critical factor in determining the possibility of breakdown and arcing once EFEE runaway has occurred. High levels of arcing are expected when the cell is coldest and there is a large adsorbed neutral density. As the cell temperature increases, the arcing will sharply decrease until at some critical temperature there will not be a sufficient neutral density to allow breakdown and the arcing rate will drop to zero. This critical temperature is a strong function of the ambient neutral density and bias voltage. Because the neutral density was not measured during the PASP Plus experiment, the effect of neutral density cannot be examined directly. In general, the ambient neutral density and plasma density are roughly correlated. Thus, it will be assumed that the neutral density will be higher at points of high ion flux. The importance of the neutral density is shown in Fig. 10, which shows the critical ambient neutral density needed for breakdown at various bias voltages and cell temperatures, with an assumed desorption cross section Q_{ESD} of 1×10^{-19} m^2, for the APSA cells. The horizontal dashed lines show the maximum and minimum neutral density for the APEX orbit generated using the EWB software. This shows that the cell temperature and expected neutral density regime of the experiment are in the area where neutral density and cell temperature dependencies would be expected. If, for example, data were gathered over the entire density range at −300 V and 220 K temperature, it would be expected that there would be arcing only above a density of approximately 1×10^{11}/m^3, whereas at 250 K arcing would only be expected to occur at points above 1×10^{13}/m^3. At approximately 275 K, the neutral density needed for breakdown exceeds that expected for the experiment, at which point no further arcing would be expected at increasing cell temperatures. In this work, the method of analysis is to examine the variation of arc rate with one parameter while keeping the remaining parameters constant. Because points of constant neutral density cannot be found, the varying neutral density for the points of constant voltage, cell temperature, and/or ion flux examined in this study can result in a large scatter in the data.

Although all of the conventional geometry cells showed a strong dependence on cell temperature for arcing, the APSA module 5 has shown the highest sensitivity to cell temperature during the experiment. Figure 11 shows the data for the arc rate variation with cell temperature for the APSA module at a voltage of −300 V and an ion flux of 1×10^{13}/m^{2}s on days 95,033–95,108. Arcing activity is seen only at the low temperatures. Because the APSA cells are thin, and the module was mounted over a cutout on the deployed panel, the temperature rise time is very fast. Thus, very few data points were taken during the times that the temperatures were transitioning from low to high. During all of the experiments at −300 V, the APSA array only showed two possible arcs at temperatures above 230 K. Because during actual operation on spacecraft the cells will only be operating in sunlight, there should not be arcing on this type of cell during most of the orbit. However, as the cells exit eclipse, they will still be cold and have a high adsorbed neutral density and the cell may arc. As they heat up, the cells will initially thermally desorb neutrals, which will further enhance the electron-stimulated desorbed neutral cloud over the triple junction and increase the chance of breakdown. Thus, the cells should initially increase their arc rate as they cross the eclipse–sunlight transition before the higher temperature of the cells reduces the arc rate. Once the high eclipse neutral density is thermally desorbed, the adsorbed neutral density will reach a steady-state value as described in the model description, which will not be high enough to lead to further breakdown. This transient effect was seen during the experiment, when increased arc rates were measured on both the silicon and APSA modules during the eclipse–sunlight transition periods.[31]

Similar temperature effects were seen on the remaining conventional geometry cells. For example, the arc rate on silicon module 2 was seen to drop to zero at approximately 260 K for experiments at −360 V and an ion flux of 1×10^{13}/m^{2}s. The nonconventional geometry cells showed very little arcing, making a study of a possible temperature dependence difficult.

The temperature dependence seen during the experiment is an important validation of the model. This temperature dependence and the eclipse–sunlight transition effect support the theory that adsorbed neutral gas is desorbed during the charging process and breaks down during the arc discharge. The other arcing models[23,25] suggest no cell temperature or eclipse–sunlight transition dependence. Because the ambient neutral density was not measured, the critical temperatures for arcing on each module cannot be properly determined. However, from the entire data set, the APSA module appears to have a critical temperature of 230 K at −300 V, whereas the critical temperature of the standard silicon arrays varies from 260 to 280 K, depending on bias voltage and ion flux.

C. Arc Rate Dependency on Ion Flux

Another important parameter in determining the arcing rate on a high-voltage solar array is the ion flux to the front surface of the array. This flux determines the ion charging time, which, along with the EFEE charging time, determines the interval between successive arcs within the radius of a discharge wave. The ion charging time is given by

$$\tau_{\mathrm{ion}} = \frac{\{V_e - [V_{\mathrm{arc}} - (\Delta Q / C_{\mathrm{front}})]\} C_{\mathrm{front}}}{e n_e v_{\mathrm{ion}} A_{\mathrm{cell}} \cos\alpha} \tag{13}$$

The term $\{V_e - [V_a - (\Delta Q/C_{\text{front}})]\}$ is the drop in potential ΔV across the coverglass due to the arc discharge. This is the potential that must be built back up by the incoming ions. The front surface capacitance is given by

$$C_{\text{front}} = \frac{1}{\left[d_1/\left(A_{\text{cell}}\epsilon_{d_1}\right)\right] + \left[d_2/\left(A_{\text{cell}}\epsilon_{d_2}\right)\right]} = \frac{A_{\text{cell}}}{\left(d_1/\epsilon_{d_1}\right) + \left(d_2\epsilon_{d_2}\right)} \tag{14}$$

The ion flux is given by $\Gamma_i = n_e v_{\text{ion}} \cos\alpha$. Thus, the ion charging time can be rewritten as

$$\tau_{\text{ion}} = \frac{\Delta V}{e\Gamma_i\left(d_1/\epsilon_{d_1}\right) + \left(d_2/\epsilon_{d_2}\right)} \tag{15}$$

Note that the cell area cancels out in the equation, and thus the ion charging time is not a function of cell area.

Given two arcing rate data points at different ion fluxes, but at the same bias voltage, the potential drop ΔV may be determined. Since the EFEE charging time is not a function of ion flux, the EFEE charging times for the two points will be the same. Thus, subtracting the two total charging times yields

$$\begin{aligned}\tau_2 - \tau_1 &= \left(\tau_{\text{ion}_2} + \tau_{\text{efee}_2}\right) - \left(\tau_{\text{ion}_1} + \tau_{\text{efee}_1}\right) \\ &= \frac{\Delta V}{e\Gamma_{i_2}\left(d_1/\epsilon_{d_1}\right) + \left(d_2/\epsilon_{d_2}\right)} \frac{\Delta V}{e\Gamma_{i_1}\left(d_1/\epsilon_{d_1}\right) + \left(d_2/\epsilon_{d_2}\right)} \\ &= \frac{\Delta V}{e\left(d_1/\epsilon_{d_1}\right) + \left(d_2/\epsilon_{d_2}\right)}\left(\frac{1}{\Gamma_{i_2}} - \frac{1}{\Gamma_{i_1}}\right)\end{aligned} \tag{16}$$

Therefore, given two charging times τ_1 and τ_2 and their corresponding ion fluxes Γ_{i_1} and Γ_{i_2}, Eq. (16) can be solved for ΔV as

$$\Delta V = \frac{e(\tau_2 - \tau_1)\left(d_1/\epsilon_{d_1}\right) + \left(d_2/\epsilon_{d_2}\right)}{\left(1/\Gamma_{i_2}\right) - \left(1/\Gamma_{i_1}\right)} \tag{17}$$

Figure 12 shows the arc rate variation with ion flux at a cell temperature of 245 K and bias voltage of −300 V. Although there is a large amount of scatter in the data at high ion fluxes, this graph clearly shows an increase in arc rate with increasing ion flux. To determine the potential drop during an arc, two arc rates need to be chosen at different ion fluxes. A fit suggested by the model of the form

$$R = \frac{1}{(C_1/\Gamma_i) + C_2} \tag{18}$$

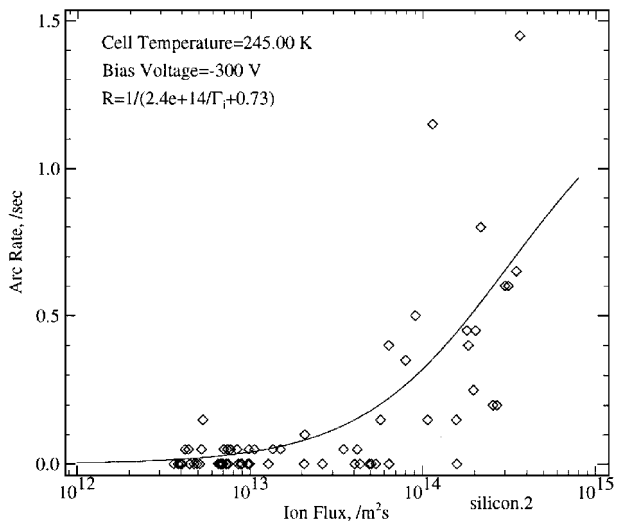

Fig. 12 Ion flux fit for silicon module 2 at 245 K and −300 V.

was used. However, because only points with a nonzero arcing rate (and thus a finite charging time) can be used, only the nonzero points were fit. The coefficient C_1 represents the parameters in Eq. (15) other than the ion flux. Using the parameters listed in Table 2 for the silicon cells and assuming the entire 300 V are discharged, a value of 2.9×10^{14} is expected for C_1. This is very close to the fit value of 2.4×10^{14}. From this fit, at an ion flux of $1.2 \times 10^{13}/\text{m}^2\text{s}$ the arc rate is 0.05/s, corresponding to a charging time of 20 s. At a flux of $2 \times 10^{14}/\text{m}^2\text{s}$, the arc rate is 0.5/s, and the charging time is thus 2 s. Substituting these values into Eq. (17) yields a potential drop during the arc of 238.8 V. Thus, the surface potential drops to −62.2 V, which is on the order of −100 V seen in ground experiments.[9]

Note that this method of estimating the potential drop is very sensitive to the arc rate and ion flux at the lower of the two ion fluxes, because these terms dominate. Typically, the point where one arc occurs is chosen, to try to make the difference in the ion fluxes greatest. Because points with only one arc have a high relative uncertainty, however, there is thus also a high uncertainty in the value of ΔV. For example, this method was used on the APSA module 5 at −300 V at a cell temperature of 215 K, resulting in a ΔV of only −45.7 V. Although this is not completely unrealistic, it is lower than expected. So, although this does help confirm the model, it is difficult to produce accurate estimates for ΔV without more accurate data.

1. *Critical Ion Flux*

For a finite experiment time τ_{exp}, there will exist a critical ion flux below which the ion charging time will exceed the experiment time. For ion fluxes below this critical flux, the electric field at the triple junction would not become sufficiently large to induce EFEE runaway during the experiment duration, and no arcing would be expected. Neglecting the EFEE charging time, the critical ion flux can be determined by setting $\tau_{\text{ion}} = \tau_{\text{exp}}$ in Eq. (13), so that

$$\Gamma_{i_{\text{crit}}} = \frac{(\Delta V)C_{\text{front}}}{eA_{\text{cell}}\tau_{\text{exp}}} \tag{19}$$

Using the parameters for the silicon cells at −300 V, assuming the potential drops to −100 V after an arc occurs, the expected critical ion flux is approximately $1 \times 10^{13}/\text{m}^2\text{s}$. If the EFEE charging time is not negligible, the critical ion flux will be greater than this value. Examination of the arc rate variation with ion flux for the silicon module 2 biased to −300 V at a temperature of 315 K yielded a critical ion flux of approximately $3 \times 10^{13}/\text{m}^2\text{s}$. Thus, since the EFEE charging time is not expected to be negligible at only −300 V, the model accurately predicts the critical ion flux. However, at the low ion fluxes the neutral density will also probably be low, which could also contribute to the lack of arcing. The critical ion fluxes seen in the PASP Plus experiment are for a 20-s experiment duration. If the modules are biased for a longer duration, a lower critical ion flux would be seen, as described by Eq. (19).

2. *Wake Effects*

When the ram angle is greater than 90 deg, the solar array modules are in the spacecraft wake. This could result in a much lower ion flux, depending on the wake angle, which would suppress arcing. Wake current collection was studied by Wang[35] for charged plates at zero, small, and large wake angles. Small wake angles are defined as $\alpha_w < \theta_0$, where θ_0 is given by $\theta_0 = \sin^{-1}(1/M)$ and M is the Mach number. When a plate at a small wake angle is biased to even a low voltage, a sheath structure develops on the plate. For the APEX orbit, the Mach angle is approximately 7–15 deg. Thus, if the ram angle is within approximately ≤105 deg and the side of the biased module is near the edge of the panel, the resulting presheath structure is able to draw a significant flux of ions to the negatively biased array. For larger ram angles, a high voltage is required to generate a high ion flux. This is case for the silicon module 2 near the edge of the panel, which is able to receive a large ion flux at low voltages when slightly in the wake and is able to receive a high ion flux at large ram angles when biased to several hundred volts. The reason that module 2 can arc in the wake at high voltages can be explained as follows.[36] In the wake, the plasma

density is reduced. Thus, the potential structure generated by a high-voltage module extends a considerable distance outward, crossing the wake boundary. This potential structure is able to deflect the ion trajectories, causing them to strike the module. If, at low wake angles and low bias voltages, the biased module is not near the leading edge, the collecting surface is not in the presheath because the front portion of the plate is unbiased. Thus, the current collected by the module in this case would be much lower. At low wake angles and high voltages, the potential structure is still able to attract ions from the wake boundary to the module, which will result in arcing. At high angles, however, the electric field at the wake boundary is too weak to draw ions to the module. This is the case for the silicon module 1, which is located half of the panel width away from the leading edge, shown in Fig. 2. Thus, it would be expected that module 2 would exhibit arcing up to ram angles of approximately 105 deg at low voltage and higher angles at high voltage, whereas module 1 should arc only in ram (i.e., $\alpha \leq 90$ deg) at low voltage and slightly into wake at high voltage. This is exactly what was seen during the experiment.[31] Module 2 was seen to arc heavily at ram angles up 120 deg and arced to a lesser degree even beyond this angle. Beyond 120 deg, the spacecraft was also in sunlight, causing the cells to be hot and further suppressing arcing. On silicon module 1, however, arcing was not observed until the panel was at a low wake angle ($\alpha \leq 105$ deg). Because operational solar panels on spacecraft have cells over the entire panel, the results seen for module 2 represent the expected arcing activity during wake operations. Thus, high-voltage solar arrays operating in the −400-V range can expect to arc heavily up to ram angles of approximately 120 deg and at lower levels beyond that.

D. Radiation Effects

The ESA on PASP Plus measured the ion and electron spectra in the 30-eV to 30-keV range. The arc rate variation with both ion and electron counts were examined to test for a possible correlation between arcing and radiation flux. A hypothesis for such a correlation is that the radiation deposits charge within the dielectrics, which would then alter the potential structure in the triple junction region and affect the arcing rate.[21] When examining the data, cell temperature, bias voltage, and plasma ion flux were all kept constant, because correlations between arcing and these parameters were all found to exist. Because the majority of the data was taken at low altitudes, where the plasma density was greatest, most of the data is at a relatively low radiation flux, making this study somewhat limited. Upon examination of the data for each of the modules, no correlation was seen to exist for either ion or electron flux. Thus, the limited data from the PASP Plus experiment indicate no correlation between arcing and radiation flux.

V. Conclusions

A semianalytic arc rate code was used to simulate the arc rates for the conventional geometry cells biased during the PASP Plus experiment. This Air Force experiment was flown aboard the APEX satellite to examine the interactions of conventional, WTC, and concentrator cell designs with the space plasma environment. Preflight predictions of the arcing activity were made with parameters generated using environmental models for the baseline APEX orbit. Postflight simulations were then conducted using the actual flight data parameters. The simulations were found to accurately predict the arcing levels seen during the experiment.

Analysis of the PASP Plus flight data was then conducted to examine arc rate dependencies on the various material, environmental, and operational parameters. The results can be summarized as follows.

1) The WTC cells were found to arc, although much less frequently than the conventional cells. The concentrator cells showed a much lower arc rate than either design, to the point to become almost indistinguishable from possible noise.

2) A strong dependency on bias voltage was found, as predicted by the model. Fits based on the model form were then made, which could then be scaled to account for differences in cell area, dielectric thickness, and work function. From this, it was verified that the arc rate varies linearly with array area and strongly with the inverse of the dielectric thickness. Onset voltages of between approximately −100 to −300 V were found for the conventional and WTC cells, which is significantly lower than was previously believed. This further shows the need to consider solar array arcing during the design of high-voltage power systems.

3) The strong dependence of arcing with cell temperature predicted by the model was also verified by the PASP Plus experiment. During eclipse, all of the conventional modules showed increased levels of arcing. The existence of a critical temperature above which no arcing was seen, for a given bias voltage and ion flux, was verified. Thus, if cells on operating power systems are kept hot, arcing can be avoided. The APSA module was mounted over a cutout on the deployed panel and was exposed to space on the back, which most closely represents the configuration of actual arrays. Because of the resulting high temperatures during sunlight, this module was found to arc almost exclusively during eclipse and transition from eclipse into sunlight. Thus, if operating systems are heated prior to exited eclipse, arcing can be significantly reduced and possibly avoided altogether.

4) Ion flux was also verified as a factor in the arcing process, with arcing possible even during wake operations. Thus, to avoid arcing, the cells must either be kept below the onset voltage or above the critical temperature.

5) Radiation flux, however, was not found to affect arcing levels, although only a limited amount of data was available to support this. The dependencies found between arcing and bias voltage, cell temperature, and ion flux, as well as the arc rate scalings with array area, dielectric thickness, and work function, all strongly support the model developed by Cho and Hastings.[14,22] The semianalytic simulation was shown to be an accurate tool for predicting solar array arcing. This tool could then be used to perform voltage/mass trade studies or to help design new cells to mitigate arcing during high-voltage operation.

References

[1]Thiemann, H., and Bogus, K., "Anomalous Current Collection and Arcing of Solar-Cell Modules in a Simulated High-Density Low-Earth-Orbit Plasma," *ESA Journal*, Vol. 10, No. 1, 1986, pp. 43–57.

[2]Stevens, N. J., *Review of Interactions of Large Space Structures with the Environment, Space Systems and Their Interactions with Earth's Space Environment*, edited by H. Garrett and C. Pike, Vol. 71, Progress in Aeronautics and Astronautics, AIAA, Washington, DC, 1980, pp. 437–454.

[3]Hastings, D. E., and Cho, M., "Ion Drag for a Negatively Biased Solar Array in Low Earth Orbit," *Journal of Spacecraft and Rockets*, Vol. 27, No. 5, 1990, pp. 279–284.

[4]Ferguson, D. C., "Solar Array Arcing in Plasma," NASA CP-3059, July 1990.

[5]Herron, B. G., Bayless, J. R., and Worden, J. D., "High Voltage Solar Array Technology," *Journal of Spacecraft and Rockets*, Vol. 10, 1973, p. 457.

[6]Miller, W. L., "An Investigation of Arc Discharging on Negatively Biased Dielectric-Conductor Samples in a Plasma," NASA CP-2359, May 1983.

[7]Kuninaka, H., "Space Experiments on Plasma Interaction Caused by High Voltage Photovoltaic Power Generation," AIAA 25th Plasmadynamics and Lasers Conf., 1994.

[8]Fujii, H., Shibuya, Y., Abe, T., Ijichi, K., Kasai, R., and Kuriki, K., "Laboratory Simulation of Plasma Interaction with High Voltage Solar Arrays," *Proceedings of the 15th International Symposium on Space Technology Science* (Kanagawa, Japan), 1986.

[9]Snyder, D. B., "Discharges on a Negatively Biased Solar Cell Array in a Charged Particle Environment," NASA CP-2359, May 1983.

[10]Kuninaka, H., "Qualitative Experiment on Arc Discharge on Negatively Biased Solar Cell," *Journal of Spacecraft and Rockets*, Vol. 27, 1990, pp. 665–668.

[11]Upschulte, B. L., Weyl, G. M., Marinelli, W., Aifer, E., Hastings, D. E., and Snyder, D., "Significant Reduction in Arc Frequency of Negatively Biased Solar Cells: Observations, Diagnostics, and Mitigation Techniques," *Journal of Spacecraft and Rockets*, Vol. 31, No. 3, 1994, pp. 493–501.

[12]Leung, P., "Characterization of EMI Generated by the Discharge of a 'Volt' Solar Array," NASA CR-176537, Nov. 1985.

[13]Snyder, D. B., "Characteristics of Arc Currents on a Negatively Biased Solar Cell Array in a Plasma," NASA TM-83728, 1984.

[14]Hastings, D. E., Cho, M., and Kuninaka, H., "The Arcing Rate for a High Voltage Solar Array: Theory, Experiments and Predictions," *Journal of Spacecraft and Rockets*, Vol. 29, No. 4, 1992, pp. 538–554.

[15]Grier, N. T., "Plasma Interaction Experiment II: Laboratory and Flight Results," NASA CP-2359, May 1983.

[16]Font, G. I., Soldi, J. D., Perez de la Cruz, C., and Hastings, D. E., "Arcing Mechanism of Wrap-Through-Contact Solar Cells," AIAA 95-0597, Jan. 1995.

[17]Grier, N. T., and Stevens, N. J., "Plasma Interaction Experiment (PIX) Flight Results," NASA CP-2071, 1983.

[18]Ferguson, D. C., "The Voltage Threshold for Arcing for Solar Cells in LEO-Flight and Ground Test Results," NASA TM-87259, 1986.

[19]Soldi, J. D., Perez de la Cruz, C., Font, G. I., and Hastings, D. E., "Arc Rate Predictions and Flight Data Analysis for the SAMPIE and PASP Plus Experiments," AIAA 95-0373, Jan. 1995.

[20]Cho, M., "Arcing on High Voltage Solar Arrays in Low Earth Orbit: Theory and Computer Particle Simulation," Ph.D. Thesis, Dept. of Aeronautics and Astronautics, Massachusetts Inst. of Technology, Cambridge, MA, 1992.

[21]Soldi, J. D., "Arc Rate Predictions and Flight Data Analysis for the Photovoltaic Array Space Power Plus Diagnostics (PASP Plus) Experiment," S.M. Thesis, Dept. of Aeronautics and Astronautics, Massachusetts Inst. of Technology, Cambridge, MA, 1995.

[22]Cho, M., and Hastings, D. E., "Dielectric Charging Processes and Arcing Rates of High Voltage Solar Arrays," *Journal of Spacecraft and Rockets*, Vol. 28, No. 6, 1991, pp. 698–706.

[23]Parks, D. E., Jongeward, G., Katz, I., and Davis, V. A., "Threshold-Determining Mechanisms for Discharges in High-Voltage Solar Arrays," *Journal of Spacecraft and Rockets*, Vol. 24, No. 4, 1987, pp. 367–371.

[24]Jongeward, G. A., Katz, I., Mandell, M. J., and Parks, D. E., "The Role of Unneutralized Surface Ions in Negative Potential Arcing," IEEE 22nd Annual Conf., NSRE, 1985.

[25]Thiemann, H., and Schunk, R. W., "Computer Experiments on Arcing Processes as Observed in Ground Tests," *Journal of Spacecraft and Rockets*, Vol. 31, No. 6, 1994, pp. 929–936.

[26]Guidice, D. A., Severance, P. S., Curtis, H. B., and Piszczor, M. F., "Investigation of Space-Environment Effects on Photovoltaic Technologies by the PASP Plus Experiment," AIAA 95-0371, Jan. 1995.

[27]Denig, W. F., "Diagnostics-LP, ESA, Emitter," PASP Plus Data Processing and Analysis Meeting, U.S. Air Force Phillips Lab., Hanscom AFB, MA, Jan. 1994.

[28]Dana, D., "Diagnostics-TPM," PASP Plus Data Processing and Analysis Meeting, U.S. Air Force Phillips Lab., Hanscom AFB, MA, Jan. 1994.

[29]Adams, S. F., "Photovoltaic Array Space Power Plus Diagnostics Flight Experiment: Pre-Flight Description of Experimental Photovoltaic Modules," U.S. Air Force Wright Lab., WL-TR-92-2080, Dayton, OH, 1992.

[30]Mong, R. L., "Arcing Mitigation and Predictions for High Voltage Solar Arrays," S.M. Thesis, Dept. of Aeronautics and Astronautics, Massachusetts Inst. of Technology, Cambridge, MA, 1993.

[31]Anon., "PASP On-Orbit Log," U.S. Air Force Phillips Lab., Hanscom AFB, MA, 1995.

[32]Delorey, D. E., "PASP Plus Time History Data Base File Structures," Boston College, Boston, MA, 1994.

[33]Davis, V. A., Gardner, B. M., McGeary, C. F., Ramos, D. A., Rankin, T. V., and Wilcox, K. G., "EWB User's Reference Manual," S-Cubed, La Jolla, CA, 1994.

[34]Ferguson, D. C., "Current Collection by the SSF Solar Array—Comparison of PASP-Plus and Sampie Results," Space Power Workshop, Albuquerque, NM, 1995.

[35]Wang, J. J., "Electrodynamic Interactions Between Charged Space Systems and the Ionospheric Plasma Environment," Ph.D. Thesis, Dept. of Aeronautics and Astronautics, Massachusetts Inst. of Technology, Cambridge, MA, 1993.

[36]Shaw, G. B., "Analysis of the Ion Current Collection in the Plasma Wake During the Charging Hazards and Wake Studies (CHAWS) Experiment," S.M. Thesis, Dept. of Aeronautics and Astronautics, Massachusetts Inst. of Technology, Cambridge, MA, 1995.

H. Anderson
Associate Editor